Exact Coherent Structures with Broken Symmetry in Plane Couette Flow

---

A Thesis
Presented to
The Division of Mathematics and Natural Sciences
Reed College

In Partial Fulfillment
of the Requirements for the Degree
Bachelor of Arts

Varchas Gopalaswamy

April 12, 2015

Approved for the Division
(Physics)

Daniel Borrero

Table of Contents

List of Figures

Introduction

> I am an old man now, and when I die and go to heaven, there are two matters on which I hope for enlightenment. One is quantum electrodynamics, and the other is the turbulent motion of fluids. And about the former, I am optimistic.
>
> Horace Lamb, 1932

Although much work has been done in understanding turbulence since Lamb's time, the twin problems of understanding the nature of turbulent transition and predicting the fine structure of turbulent flows after development remain unsolved to this day, having vexed scientists and engineers in much the same way a plucky band of Gauls did for Caesar. Flow states are said to be **turbulent** if they display large spatiotemporal variations in fluid velocity, as in Figure 1. Understanding turbulence is vitally important, since turbulent flows appear in man-made scenarios such as the flow around ships or aircraft, as well as in natural scenarios like the atmosphere of Jupiter and the flow of blood in the heart. The degree to which a flow is turbulent is characterized by the **Reynolds number**(Re) , which is the (dimensionless) ratio between the inertial and viscous damping forces. At small Re, **viscosity** of a fluid (which is analogous to fluid friction) dominates, and smooths out large velocity gradients in the fluid, resulting in the well-ordered **laminar** flow. At large Re, kinetic energy is dissipated at a lower rate, allowing for the existence of increasingly complex flow structures, such as eddies or vortices, which are typical of turbulence.

Plane Couette Flow

Since viscosity is a dissipative force, a viscous fluid that has no energy input will eventually have all of its kinetic energy dissipated into internal energy. Therefore, sustaining turbulence requires some form of constant energy input, which in the case of plane Couette flow (Figure 2), is provided through the shear stress of the constantly moving parallel plates. The geometry of the plane Couette system is extremely simple, with only one geometrical parameter h, the half-distance between the parallel plates,

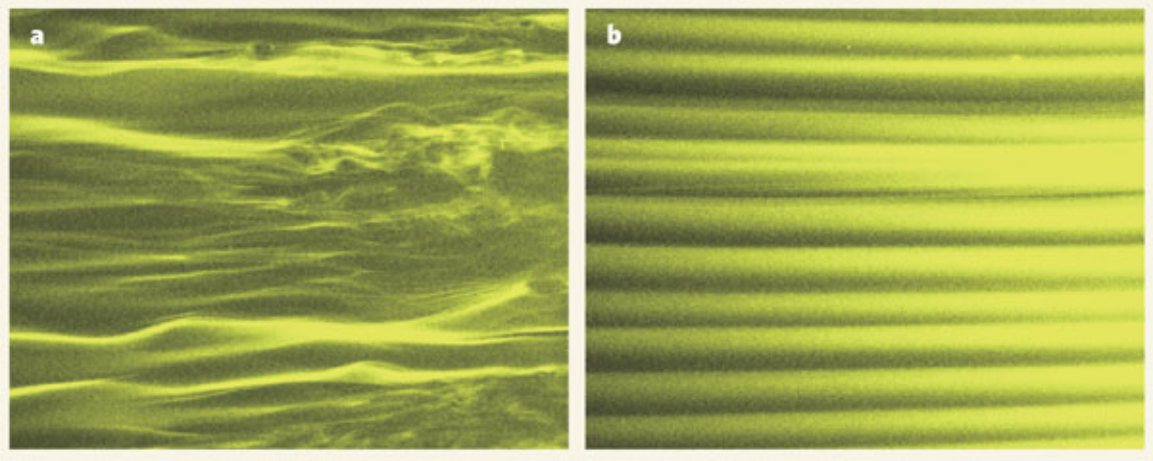

Figure 1: Streamlines on two surfaces of differing smoothness showcase the difference between laminar and turbulent flows. (a) In turbulent flow across an extremely smooth surface, streamlines break up into chaotic eddies and swirls, while in (b), the laminar flow across a rough surface preserves the streamlines. Reproduced from K.S. Choi, "Fluid Dynamics: The rough with the smooth", *Nature*, vol. 440, no, 7085, pp. 754-754, 2006 [1].

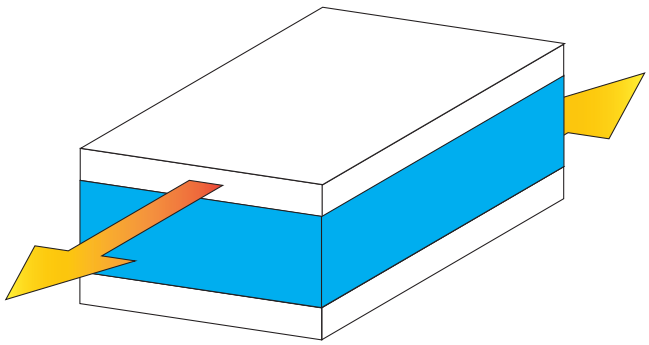

Figure 2: A schematic of the plane Couette geometry. The upper and lower plates (white) extend infinitely in the plane, as does the fluid (blue) filling the gap between. The upper and lower plates move with some constant velocity, and apply shear stresses on the fluid, resulting in fluid motion. While in general the plates can move in any direction, there is always a reference frame in which the plates move with equal but opposite velocity, and it is convenient to work in this reference frame. According to convention, the x axis is aligned along the plate velocity, and is referred to as the **streamwise** direction. The y-axis is aligned perpendicular to the plates and is referred to as the **wall-normal** direction. The z-axis is normal to both axes and is referred to as the **spanwise** direction.

and one kinematic parameter V, the constant velocity of the upper plate[1], giving the

[1]While in principle the upper and lower plate can have different velocities, there is always a reference frame in which the upper plate has velocity V, and the lower plate has velocity $-V$.

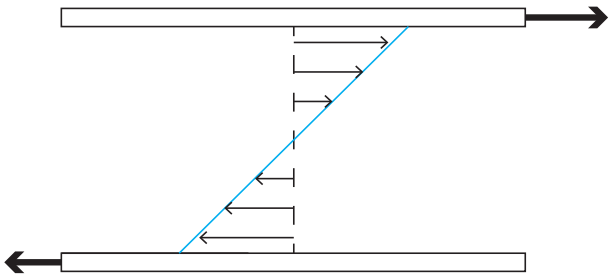

Figure 3: A cross-sectional representation of plane Couette flow, with the linear, laminar velocity profile shown. By symmetry, the laminar profile must be the same everywhere. At the top and bottom, where the fluid meets the walls, no-slip boundary conditions require that the wall-tangent velocity equal the boundary velocity.

Reynolds number as

$$Re = \frac{hV}{\nu}, \tag{1}$$

where ν is the kinematic viscosity. When Re is very small, only the laminar flow state is stable. In the case of plane Couette flow, this corresponds to the linear velocity profile shown in Figure 3. As Re increases, experiments [5] have demonstrated the existence of long-lived turbulent flows, even though linear stability analysis indicates that the laminar state remains stable.

Tackling Turbulence

The traditional approach for the analysis of turbulent flow is the statistical approach initially developed by Reynolds, Prandtl, von Karman, Kolmogorov and others [6]. At the core of the statistical approach to turbulence is the assumption that turbulent flow states can be expressed as random perturbations around some mean flow. At high Re, where direct numerical simulation (DNS) of the flow is computationally infeasible[2] , the statistical approach is invaluable, but at low-to-moderate Re, these models can become less accurate [6]. Even ignoring the moderate Re behavior of the statistical models, the fundamental issue with the statistical approach is its discarding of the dynamical information about turbulence. Methods like Reynolds Averaged Navier-Stokes use a combination of time-averaging and modeling to eliminate small scale perturbations, while Large Eddy Simulations explicitly do not resolve small scale structures, and choose instead to model them. For this reason, it seems likely that while statistical methods are fundamental to applied computational fluid dynamics (CFD), especially in engineering practice, they cannot truly provide an answer to the turbulence problem.

An alternate approach was proposed by Eberhard Hopf in 1948 [7]. Hopf suggested that solutions to the Navier-Stokes equations might be thought of as trajectories in an

[2]In essence, this is due to the fact that the minimum computational resolution required for DNS scales as $Re^{3.5}$ in 3D.

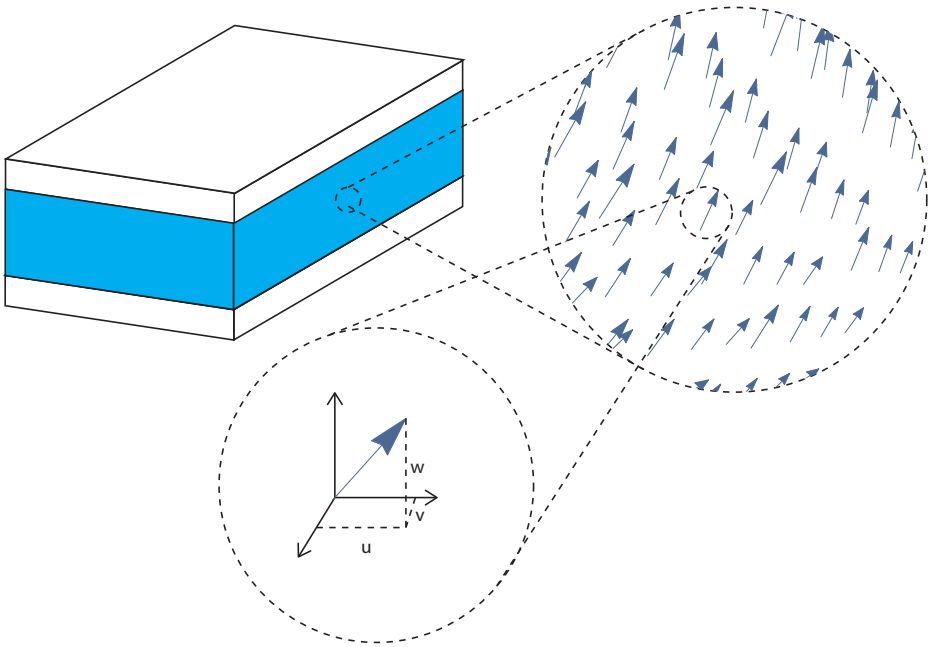

Figure 4: At each point in the fluid volume, the velocity field has a value that is described by three numbers, thus requiring three dimensions to track over time.

infinite dimensional state space in which each point corresponded to a possible velocity field. To better understand what this would mean, consider the mean velocity field of some infinitesimal volume of fluid, pictured in Figure 4. In order to describe the velocity vector, three numbers are required (each of which can take any real value), so this vector lives in a three dimensional vector space. Now any finite fluid volume will have an uncountably infinite number of points at which the velocity field has a value, so we would need an uncountably infinite set of numbers to describe any velocity field. An object that would keep track of all these numbers would form an infinite dimensional vector $\mathbf{v} = \{v_{i,1}, v_{i,2}, v_{i,3}...\}$, $i \in \mathbb{R}$, so that any flow state can be represented by a particular vector in this infinite dimensional vector space, known as the **state space**. Luckily, every point in the space does not necessarily correspond to a solution of the Navier-Stokes equation; for a given finite Re, for instance, the gradient of the velocity field cannot be too large. Hopf thus conjectured that physical trajectories, corresponding to solutions to the Navier-Stokes equation would lie on some finite-dimensional manifold (known as the **inertial manifold**) embedded within this infinite dimensional space. The restriction of dynamics from the infinite dimensional space to a finite dimensional inertial manifold due to the variation of a control parameter has been rigorously proven under certain conditions [8]. For the Navier-Stokes equation, the inertial manifold's control parameter[3] is Re, and physical intuition suggests that its structure should also have Re dependence, since at very low

[3]The control parameter of a dynamical system is a number that is time-independent, and typically dictates the behavior of the system in some way. For instance, in the dimensionless simple harmonic oscillator, $\ddot{x} + 2\zeta\dot{x} + x = 0$, the control parameter is the dimensionless number ζ, whose value determines whether the system is undamped, underdamped, over damped or critically damped.

Re, the only physical solution is the laminar state (which corresponds to the origin of the state space). As *Re* increases, more complex flows become physically permissible, so the inertial manifold grows from a point of dimension 0 into a more complex, higher dimensional manifold. Hopf proposed that turbulence in this view was simply a trajectory that would travel across wide distances on the inertial manifold.

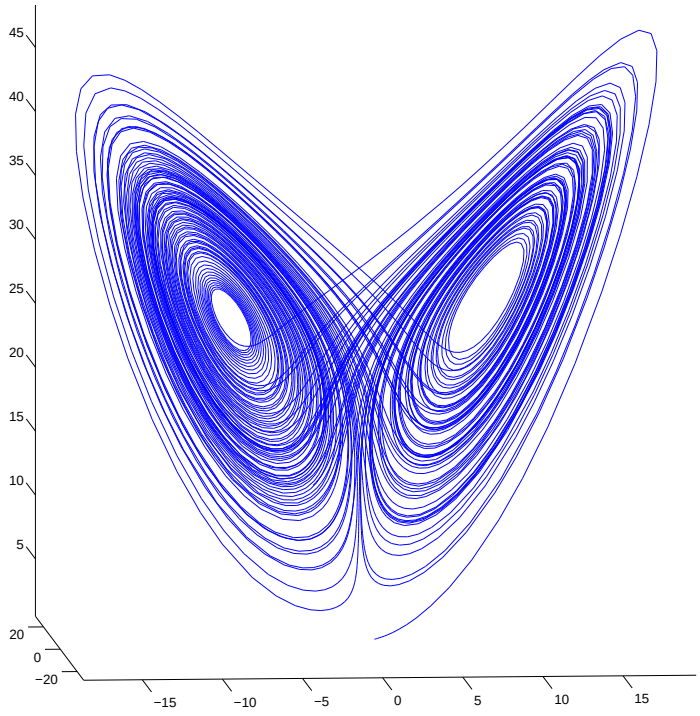

Figure 5: A plot of a particular trajectory around the Lorenz attractor. The Lorenz system is an excellent example of a system in which the dynamics exist on a sub-manifold - in this case, the space is reduced from three dimensions to the (fractal) dimension of 2.06 [2].

Unfortunately for Hopf, the computer power necessary to pursue this line of work was not available in 1948, leading him to comment in frustration that "the great mathematical difficulties of these important problems are well known and at present the way to a successful attack on them seems hopelessly barred" [7]. It would take until 1963 and the derivation of the Lorenz attractor (Figure 5) for the first numerical state-space analysis of turbulence [9], albeit for a highly truncated version

of Navier-Stokes, designed to investigate Rayleigh-Bernard convection[4]. There have also been a number of efforts to explore the structure of invariant manifolds in moderate turbulence Navier-Stokes, such as Proper Orthogonal Decomposition [10] and the 'self-sustaining process theory' [11], which while fruitful, are nevertheless models of turbulent flow, and not an exact analysis of Navier-Stokes.

Another avenue of research emerged in 1990, when Nagata computed nontrivial

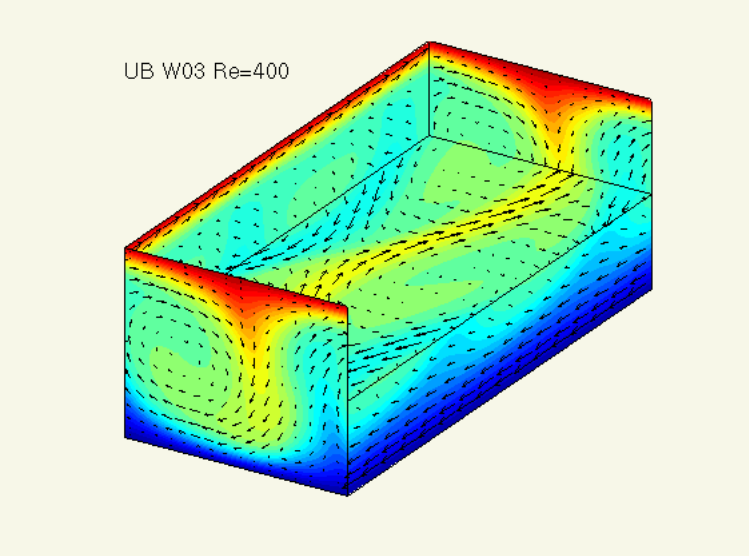

Figure 6: The roll-streak structure of the Nagata upper branch equilibrium [3]. The vortex that forms the roll is clearly visible on the box wall, as is the streak running through the midplane of the box. Solutions that approach the vicinity of this solution in the state space will take on some of this roll-streak structure.

equilibrium flow states for plane Couette flow by continuing the wavy vortex solution of Taylor-Couette flow [3]. This class of solutions, which were named **exact coherent structures** by Waleffe [12] are the result of calculating exact, invariant solutions of the fully resolved Navier-Stokes equations. The family of exact coherent structures was expanded with the discovery of **traveling wave equilibria** by Nagata in 1997, the computation of **periodic orbits** by Kawahara and Kida in 2001 [13], and the computation of **relative periodic orbits**[5] by Viswanath in 2007 [14]. Figure 7 summarizes the four categories of exact coherent structures.[6] The ultimate hope of this line of research is that turbulence can be viewed as chaotic trajectories on the inertial manifold that are guided by exact coherent structures (Figure 8).

Of the work that has been done in the field, a large proportion of it has been computational, and experiments by Hof and de Lozar [15] are at present the only

[4]Interestingly, Lorenz truncated Navier-Stoke via a Galerkin approximation, which is what the simulation library `Channelflow` which features heavily in this thesis also does, though it allows for many more Fourier modes than Lorenz did.

[5]That is, flow states that are periodic after some phase shift

[6]VG 4/8: If I explain that in Figure 8, should I replicate that here?

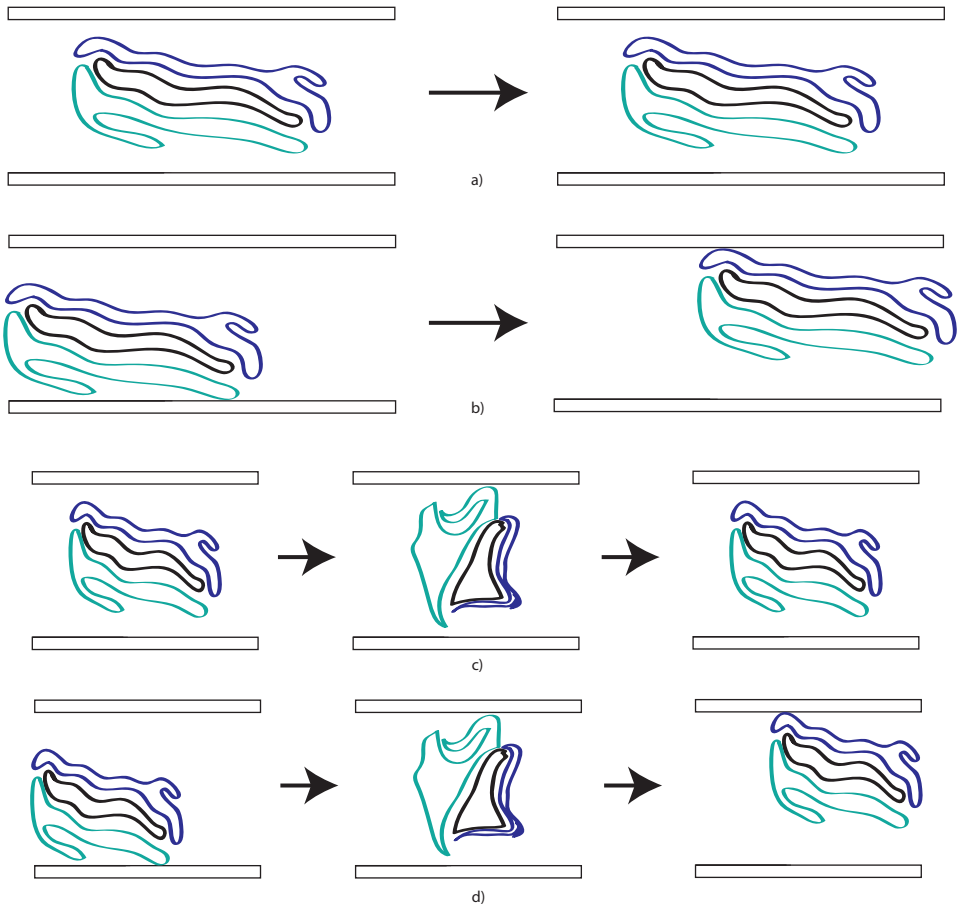

Figure 7: The four main categories of exact coherent structures. In all diagrams, only a particular velocity structure of the flow state is displayed, to demonstrate the particular type of exact coherent structures. (a) An equilibrium solution, where the fluid structure does not change over time. (b) A relative equilibirum or travelling wave solution, where the state does not change in its own reference frame, but is translated relative to the observer. (c) A periodic orbit, where the flow state changes over time, but returns to the original state after some period T. (d) A relative periodic orbit, where the flow state is periodic in its own reference frame, but is translated relative to the observer.

direct experimental verifications for the existence of exact coherent structures in nature. However, indirect results, such as the resemblance of Nagata's so-called 'upper branch' equilibrium solution [3] to the roll-streak structure seen in DNS [16] (Figure 6, and the potential role of the stable manifold of the lower branch solution in separating the turbulent and laminar basins of attraction [12] suggest that exact coherent structures likely play a fundamental role in the behavior and evolution of turbulent flow states. Advances in computing power, along with the development of CFD algorithms such as Channelflow [17] have also made the computation of these structures generally feasible. In order to compute the first generation of exact coherent structures, researchers placed substantial symmetry constraints were placed upon the dynamics.

This had the benefit of greatly reduced computational cost, but has resulted in exact coherent structures that are not necessarily representative of turbulence, since we expect turbulent fields to display little to no symmetry in general. As a result, while the symmetric exact coherent structures appear to inform our understanding of turbulent transitions [18], they do not necessarily inform our understanding of turbulent dynamics. The focus of this thesis has been to investigate the properties of periodic orbits with broken symmetry, and how they compare to their unbroken brethren.

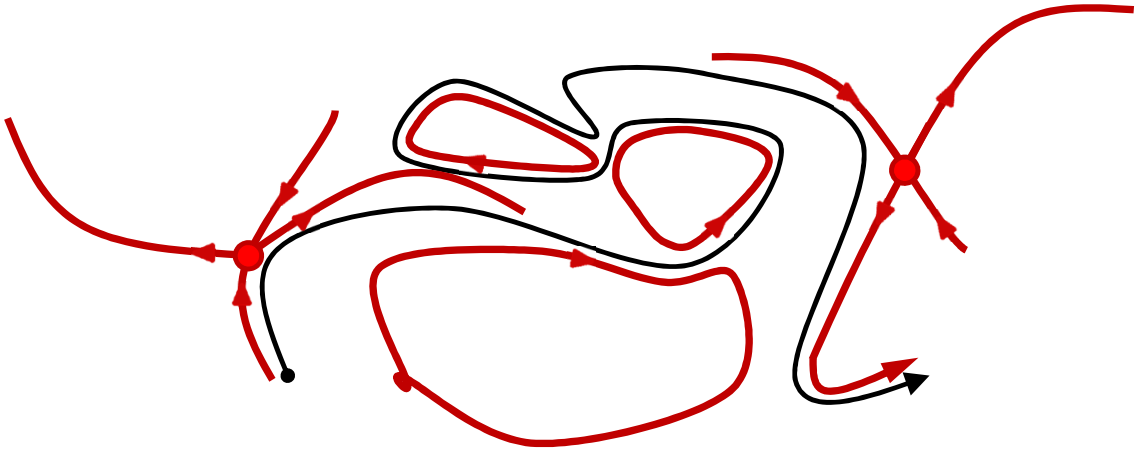

Figure 8: A schematic of a 2D projection of a turbulent trajectory, and the coherent structures that guide it. (a) A turbulent trajectory in black appears chaotic and unpredictable in isolation. (b) When the underlying coherent structures in red are superimposed, however, the guiding of the dynamics by the exact coherent structures becomes evident. Starting from the left, the trajectory is pulled in towards an equilibrium (filled circle) along a stable manifold (arrow pointing inwards), before being ejected along an unstable manifold (arrow pointing outwards). The trajectory then shadows three periodic orbits, whose stable and unstable manifolds are not trivial to visually represent, but nonetheless exist, before being attracted and ejected by the final equilibrium, after which the trajectory may continue to remain turbulent, or may relaminarize. Reproduced from D. Borrero, *Subcritical Transition to Turbulence in Taylor-Couette Flow*, PhD. Dissertation, Dept. of Physics, Georgia Institute of Technology, 2014 [4].

In the first chapter, I will lay out the Navier-Stokes equation and problem geometry in further detail. In the second chapter, I will discuss the symmetries of the Navier-Stokes equations for plane Couette flow and the advantges and disadvantages afforded by considering symmetric subspaces. The third chapter will discuss in detail the spectral methods used to integrate Navier-Stokes forward in time and the Newton-Krylov-hookstep algorithm used to find coherent structures in Channelflow, along with the workflow used in this thesis. Chapter 4 presents the results of this thesis, which includes a low period orbit with broken symmetry over a large range of Reynolds numbers. Chapter 5 provides a summary of this thesis and suggests potential topics for future research.

Chapter 1

Equations of Flow

For every action, there is an equal and opposite regulatory body.

Anonymous

1.1 Formalisms

If we were to describe the dynamics of a point particle, we would begin with Newton's Second Law,

$$\frac{\mathrm{d}\mathbf{p}}{\mathrm{d}t} = \mathbf{F}, \tag{1.1}$$

and writing down the body force as a function of position, time, etc. The trajectory could then be calculated via analytic or numeric integration of (1.1). While in principle we can use this approach to describe the behavior of a large collection of particles making up the fluid, practical considerations prevent us from modeling the behavior of each individual particle, for the following reason – in a milliliter of water, there are approximately 10^{22} molecules of water, each with 6 degrees of freedom[1]. Applying (1.1) to all these particles would result in about 10^{23} coupled ordinary differential equations. Such a set of equations would be hard to write down, let alone solve! Clearly, a more intelligent approach is needed – the formalism that I will present here begins by modeling the fluid as a continuum. My derivation is based off that in [19].

1.1.1 The Eulerian Formulation

When asked to consider the mechanical evolution of some collection of bodies, two obvious methods would be readily apparent - we could either follow a collection of particles on their way through space and time (the **Lagrangian** formulation), or we could situate ourselves at some point in space and observe the properties of

[1] If we ignore the vibrations of the O-H bonds

particles that pass through the surrounding region (the **control volume**) over time (the **Eulerian** formulation). The Lagrangian formulation will be familiar to anyone with a basic physics education, since it lends itself readily towards analysis of rigid-body motion. When considering fluids, however, the disadvantages of the Lagrangian formulation (noted above) stand in contrast to the ease of analysis afforded by the Eulerian formulation, which remains as easy (or hard) as it was for rigid body motion. For this reason, I will focus on the Eulerian formulation of fluid mechanics in this thesis.

1.1.2 The Fluid Particle

A consequence of the Eulerian formulation is that we cannot know the full timeline of any individual particle over its lifetime – we only know the properties of particles within the control volume. Therefore, the principle quantity in the Eulerian formulation is the velocity field[2] $\mathbf{v}(\mathbf{x},t) = v_x(\mathbf{x},t)\hat{\mathbf{x}} + v_y(\mathbf{x},t)\hat{\mathbf{y}} + v_z(\mathbf{x},t)\hat{\mathbf{z}}$, along with the pressure and density fields, which are the average values of the property in a control volume surrounding a point. A subtle issue arises in doing this, however. Since the velocity field is continuous, it has a well-defined value at every point in space, which we would want to be associated with the velocity of a particle at that point in space. However, there are finite number of particles in any collection of fluid with a finite spatial extent. If these particles have some finite volume, then the formulation assigns multiple velocities to a single particle - and if the particles are infinitesimal, then the formulation assigns velocities to empty space! This issue can be resolved by appealing to the continuum hypothesis, which suggests that a control volume (the '**fluid parcel**') can be chosen such that it is large enough to form a meaningful average of the quantities within, but small enough that the properties do not vary significantly over the parcel, and that from a macroscopic perspective, the properties appear continuous. The reader may ask "Can such a parcel even exist?". As an example, let us consider water, with approximately 10^{22} molecules per cubic centimeter. Imagine our fluid parcels as tiling the volume with cubes of length dl, giving a total volume of dl^3 per parcel. First, let us make dl small enough that the macroscopic properties appear continuous - how about one micron? That gives the volume of a fluid particle as one cubic micrometer. For scale, consider that the volume of the human red blood cell ranges from 80-100 cubic micrometers [20] - this seems acceptably small for considering, say, the flow around a ship.[3] The number of water molecules within each fluid parcel is then

$$10^{22}dl^3 = 10^{22} \times 10^{-12} = 10^{10}, \tag{1.2}$$

or about 10 billion water molecules, which is certainly sufficient to achieve a meaningful average. Having defined a fluid parcel in this way allows us to behave as if these macroscopic variables have well-defined values at every point in space, which greatly simplifies the following analysis.

[2] As opposed to particle trajectories $\mathbf{x}(t)$ in the Lagrangian formulation.

[3] The validity of the continuum hypothesis is clearly dependent on the density of the fluid and the length scale of the phenomenon to be modeled, but holds up even for the sparse gas clouds of protoplanetary disks [21].

1.2 Mass Conservation

While not formally a part of the Navier-Stokes equation (which is a statement about conservation of linear momentum), conservation of mass is nevertheless essential in solving fluid problems, and will serve as a demonstration of the control volume method. Consider a volume Ω which is fixed in space, and has some mass density $\rho = \rho(\mathbf{x}, t)$ and some fluid velocity $\mathbf{v} = \mathbf{v}(\mathbf{x}, t)$ that are generically functions of time and space, allowing us to define the **mass current density** $\mathbf{m} = \mathbf{v}\rho$. The mass contained within the volume Ω is then given by

$$M = \int_\Omega \rho \ dV. \tag{1.3}$$

The flow of mass out of the volume through the surface $d\Omega$ of Ω is given by

$$\mathcal{M}_{flow} = \int_{d\Omega} \mathbf{m} \cdot \mathbf{n} \ dA = \int_\Omega \nabla \cdot (\rho \mathbf{v}) \ \ dV, \tag{1.4}$$

by the divergence theorem. Now in classical physics, mass should not appear or disappear, so the sum of the rate of mass flow into (or out of) the volume and the rate of change of mass inside the volume M_{encl} must be zero, giving

$$\frac{\partial M_{encl}}{\partial t} + \mathcal{M}_{flow} = 0, \tag{1.5}$$

$$\frac{\partial}{\partial t}\left(\int_\Omega \rho \ dV\right) + \int_\Omega \nabla \cdot (\rho \mathbf{v}) \ \ dV = 0, \tag{1.6}$$

but since Ω is time-independent, the time derivative commutes with the integral, giving

$$\int_\Omega \frac{\partial \rho}{\partial t} + \nabla \cdot (\rho \mathbf{v}) \ \ dV = 0. \tag{1.7}$$

Since Ω is arbitrary, the integrand must be zero everywhere, so mass is conserved if

$$\frac{\partial \rho}{\partial t} + \nabla \cdot (\rho \mathbf{v}) = 0. \tag{1.8}$$

If the flow is (approximately) incompressible, which will be true for small Mach numbers[4], then ρ must be constant, and (1.8) becomes

$$\nabla \cdot \mathbf{v} = 0, \tag{1.9}$$

for both steady and unsteady flows.

[4]The Mach number is the ratio of the fluid velocity to the speed of sound in the fluid. For reference, the speed of sound in water is 1497 ms^{-1} at room temperature and pressure. I figured this tidbit should stick around so the fourth reader has a sense of scale for the whole thing.

1.3 Conservation of Linear Momentum

As mentioned earlier, the Navier-Stokes equations are simply a statement of conservation of linear momentum, along with certain assumptions about stress and strain, which are presented below.

1.3.1 Stress

Stress is a mathematical entity that contains information about the forces acting over an object. As with force, we define positive stress as stress that acts towards the control volume, and negative if they act away. Unlike force however, stress is not a vector, since it encodes both the force on an object, as well as the plane that force acts in. Since there are three directions and three planes of action, a stress entity generally has nine elements, and can be represented as a **second rank tensors**. For example, the viscous stress tensor $\mathcal{T}$ is identified by two subscripts, where the first subscript indicates the plane of action, and the second the direction of action. So $\mathcal{T}_{xy}$ would represent the viscous force on the (y, z) plane acting in the y direction.

1.3.2 Strain

Now that we can consider the forces on a fluid particle, we need to link these forces back to the observable quantities in the form of strain, a second rank tensor which encodes information about the deformation of the continuum. In solids, this is easy - Hooke's Law for elastic substances, for instance, sets the strain proportional to the stress:

$$\sigma = \mathcal{C}\epsilon, \tag{1.10}$$

where σ is the Cauchy stress tensor, $\mathcal{C}$ is the (fourth rank) stiffness tensor and ϵ is the infinitesimal strain tensor. However, for fluids, this is not the case - you can imagine that if you applied a constant force to a cube of water, it would deform continuously, without offering any resistance. Newton theorized that for continuously deformable fluids, the 1-D relationship between stress $\mathcal{T}$ and strain $\mathcal{S}$ should have the following form:

$$\mu\frac{\mathrm{d}\mathcal{S}}{\mathrm{d}t} = \mu\frac{\mathrm{d}u}{\mathrm{d}x} = \mathcal{T}, \tag{1.11}$$

where μ is the fluid viscosity and u is the velocity. Stokes extended this to three dimensions, giving the Newtonian constitutive relationship between stress and strain (for an incompressible fluid):

$$\mathcal{T}_{ij} = -P\delta_{ij} + \mu\left(\frac{\partial u_i}{\partial x_j} + \frac{\partial u_j}{\partial x_i}\right), \tag{1.12}$$

where δ_{ij} is the Kronecker delta function[5] and P is the pressure. A fluid obeying Newton's constitutive relation is called a Newtonian fluid. Water, and most gases under normal conditions are Newtonian, but fluids like blood, quicksand and corn starch (to name a few) are not.

[5] $\delta_{ij} = 1$ if $i = j$ and 0 otherwise

1.3.3 Surface Forces

Having written down the stress tensor $\mathcal{T}$ as a function of the velocity field, we can now link it to the surface forces on a fluid particle. Recalling that stresses act over $d\Omega$ of the fluid particle, the total force is then simply

$$\mathbf{F} = \int_{d\Omega} \mathcal{T} \cdot \mathbf{n} \; dA, \tag{1.13}$$

where $\mathbf{n}$ is the surface normal.

1.3.4 Newton's Second Law

For a fluid parcel Ω, Newton's Second Law can be rewritten as

$$\sum \mathbf{F} = \int_{\Omega} \frac{\partial \rho \mathbf{u}}{\partial t} \; dV \tag{1.14}$$

where the sum is over all possible external forces. We can further split $\mathbf{F}$ into two kinds of forces - body forces, like gravity or electromagnetism, and surface forces due to stresses. We group the body forces $\mathbf{F}_b$ as

$$\mathbf{F}_b = \int_{\Omega} \rho \mathbf{f} \; dV, \tag{1.15}$$

where $\mathbf{f}$ is the **body force density**. Using (1.13) to express the surface forces, (1.14) becomes

$$\int_{\Omega} \rho \mathbf{f} - \frac{\partial \rho \mathbf{u}}{\partial t} \; dV + \int_{d\Omega} \mathcal{T} \cdot \mathbf{n} \; dA = 0. \tag{1.16}$$

This can be written in differential form using the same trick used to generate (1.8), giving Cauchy's Equation of Motion

$$\rho \mathbf{f} - \frac{\partial \rho \mathbf{u}}{\partial t} + \nabla \cdot \mathcal{T} = 0. \tag{1.17}$$

From this, the incompressible Navier-Stokes equation arise by a substitution of (1.12) into (1.17), giving (after tedious rearrangement by components),

$$\frac{\partial \mathbf{u}}{\partial t} + (\mathbf{u} \cdot \nabla)\, \mathbf{u} = \mathbf{f} - \frac{1}{\rho} \nabla P + \frac{\mu}{\rho} \nabla^2 \mathbf{u}. \tag{1.18}$$

By using the substitutions

$$\mathbf{x} \Rightarrow L\mathbf{x} \tag{1.19}$$

$$\mathbf{u} \Rightarrow U\mathbf{u} \tag{1.20}$$

$$t \Rightarrow \frac{L}{U} t \tag{1.21}$$

$$P \Rightarrow \rho U^2 P, \tag{1.22}$$

and neglecting body forces, we obtain the nondimensional version of (1.18) –

$$\frac{\partial \mathbf{u}}{\partial t} + (\mathbf{u} \cdot \nabla)\,\mathbf{u} = -\nabla P + \frac{1}{Re}\nabla^2 \mathbf{u}, \tag{1.23}$$

$$\nabla \cdot \mathbf{u} = 0, \tag{1.24}$$

where

$$Re = \frac{UL\rho}{\mu}. \tag{1.25}$$

In practice, the values of L and U are chosen by convention to reflect the natural scales of the problem at hand.

1.4 Plane Couette Flow

Since plane Couette flow is a shear driven flow, we set the pressure gradient to zero and use no-slip boundary conditions at the walls, which sets the surface tangential velocity equal to the surface velocity. The Navier-Stokes equation for plane Couette flow is then given by

$$\frac{\partial \mathbf{u}}{\partial t} + (\mathbf{u} \cdot \nabla)\,\mathbf{u} = \frac{1}{Re}\nabla^2 \mathbf{u}, \tag{1.26}$$

with boundary conditions

$$\mathbf{u}(x, \pm 1, z, t) = (\pm 1, 0, 0)\,, \tag{1.27}$$

and geometry as pictured in Figure 2. We nondimensionalize by the velocity V of either plate and the half-plate distance h, with the Reynolds number

$$Re = \frac{hV\rho}{\mu}. \tag{1.28}$$

In order to derive the laminar velocity profile shown in Figure 3, note that at very low Re, the right hand side of (1.26) dominates. If we assume that the flow is unidirectional and steady, so that $\mathbf{u} = u_x \hat{\mathbf{x}}$, symmetry considerations tell us that the velocity field can only be a function of height, so that the Navier-Stokes equation reduces to

$$\frac{\partial^2 u_x}{\partial y^2} = 0. \tag{1.29}$$

This has a solution of the form

$$\mathbf{u}(y) = y\hat{\mathbf{x}}, \tag{1.30}$$

which corresponds to the laminar flow profile in Figure 3. Consider then a perturbation $\mathbf{v}(x, y, z, t)$ from this laminar state, so that the initial field is $\mathbf{u}(x, y, z, t) = \mathbf{v}(x, y, z, t) + y\hat{\mathbf{x}}$. Substituting this into (1.23), we get

$$\frac{\partial \mathbf{v}}{\partial \tau} + y\frac{\partial \mathbf{v}}{\partial x} + v\hat{\mathbf{x}} + \mathbf{v} \cdot \nabla\,\mathbf{v} = \frac{1}{Re}\nabla^2 \mathbf{v}, \tag{1.31}$$

$$\nabla \cdot \mathbf{v} = 0, \tag{1.32}$$

with the usual no-slip boundary conditions

$$\mathbf{v}(x, \pm 1, z, t) = 0, \tag{1.33}$$

as well as artificial boundary conditions

$$\mathbf{v}(x, y, z, t) = \mathbf{v}(x + L_x, y, z, t), , \tag{1.34}$$
$$\mathbf{v}(x, y, z, t) = \mathbf{v}(x, y, z + L_z, t), , \tag{1.35}$$

where L_x and L_z are the lengths of the periodic cell. The artificial boundary conditions are necessary to render the infinite planar domain into a computationally tractable form. This gives the complete equation of motion for the perturbing velocity field. Since the laminar profile is steady, understanding the turbulent field's trajectory in state space now reduces to understanding the behavior of the turbulent perturbation, and the structure of its inertial manifold.

Chapter 2

Symmetry in plane Couette flow

Tyger! Tyger! Burning bright,
In the forests of the night.
What immortal hand or eye,
Could frame thy fearful symmetry?

William Blake, *The Tyger*

Dynamical systems in physics often display symmetry. The electron wavefunction in the ground state of hydrogen, or the gravitational motion of a planet around a star, for instance, display very high degrees of spatial symmetry. Understanding the symmetries of a system can be incredibly useful to an investigator, since they hint at conserved physical quantities (through Noether's Theorem), and can greatly reduce the complexity of the system in various ways. But first, some definitions:

Definition 1. [22] A **group** $(G, *)$ is an object that contains a set G and a binary operator known as the **group law** $* : G \times G \to G$ that has the following properties

1. **Closure**: For every $a, b \in G$, $a * b \in G$,
2. **Associativity**: For every $a, b, c \in G$, $a * (b * c) = (a * b) * c$,
3. **Identity**: There exists a the unique identity $e \in G$ such that for any $a \in G$, $e * a = a$,
4. **Inverse**: For all $a \in G$, there exists an inverse $a^{-1} \in G$ such that $a * a^{-1} = a^{-1} * a = e$.

and has a group action $\star : G \times A \to A$ on a set A such that

1. **Associativity** For all $a, b \in G$ and $\alpha \in A$, $a \star (b \star \alpha) = (a * b) \star \alpha$,
2. **Identity** For all $\alpha \in A$, $e \star \alpha = \alpha$.

Definition 2. The **order** of a group $(G, *)$ is the number of elements in G.

Definition 3. A **subgroup** $(H, *)$ of $(G, *)$ is a group such that $H \subseteq G$.

Definition 4. A **symmetry group** for a dynamical system $\dot{\mathbf{x}} = \mathbf{f}(\mathbf{x})$ is the group $(\Sigma, *)$ such that for any linear transformation $\sigma \in \Sigma$,

$$\sigma \star \dot{\mathbf{x}} = \sigma \star \mathbf{f}(\mathbf{x}) = \mathbf{f}(\sigma \star \mathbf{x}). \tag{2.1}$$

Such a linear transformation is said to be a symmetry transformation, and the dynamical system is then said to be **Σ-equivariant**.

Definition 5. For a particular state $\mathbf{u}$ in a dynamical system $\dot{\mathbf{x}} = \mathbf{f}(\mathbf{x})$, a symmetry group $(\Sigma, *)$ such that for all $\sigma \in \Sigma$,

$$\sigma \mathbf{u} = \mathbf{u} \tag{2.2}$$

is known as the **isotropy subgroup** of $\mathbf{u}$, and $\mathbf{u}$ is said to **satisfy** or be **fixed** by Σ.

Definition 6. If a group $(G, *)$ has the further property that for all $a, b \in G$, $a * b = b * a$, then the group is **abelian**

Definition 7. Two subgroups $(J, *)$ and $(H, *)$ of $(G, *)$ are considered **conjugate** if for some $a \in G$,

$$a * J * a^{-1} = H. \tag{2.3}$$

A set of mutually conjugate groups makes up a **conjugacy class**, and since the action of members of a conjugacy class on a particular state $\mathbf{u}$ can be considered equivalent, only one representative member of a conjugacy class needs to be considered.

Definition 8. A set $\mathcal{G}$ is said to **generate** a group $(G, *)$ if repeated applications of the group law between elements of $\mathcal{G}$ produced all the elements of G.

The symmetry relations of plane Couette flow are discussed extensively in [23, 18], which I will present here for the sake of flow[1]. To keep things terse, the group action and group law operator is omitted and can be inferred from context, and a group $(G, *)$ is referred to by the set G.

2.1 Unbounded Navier-Stokes

If we do not impose boundary conditions on the 3D Navier-Stokes equations on an infinite domain, the system will be equivariant under the group of continuous rotational and translational symmetry transformations, as well as the discrete **pointwise inversion** symmetry transformation σ_{xz} [24], which has the following action on the system:

$$\sigma_{xz}\mathbf{u}(\mathbf{x}) = -\mathbf{u}(-\mathbf{x}) \tag{2.4}$$

While the rotation or translation transformation can be easily conceptualized, the pointwise inversion transformation can provide some difficulty. The easiest way of visualizing the transformation is to view it in a 2D domain instead of in the full 3D, as shown in Figure 2.1.

[1] haha

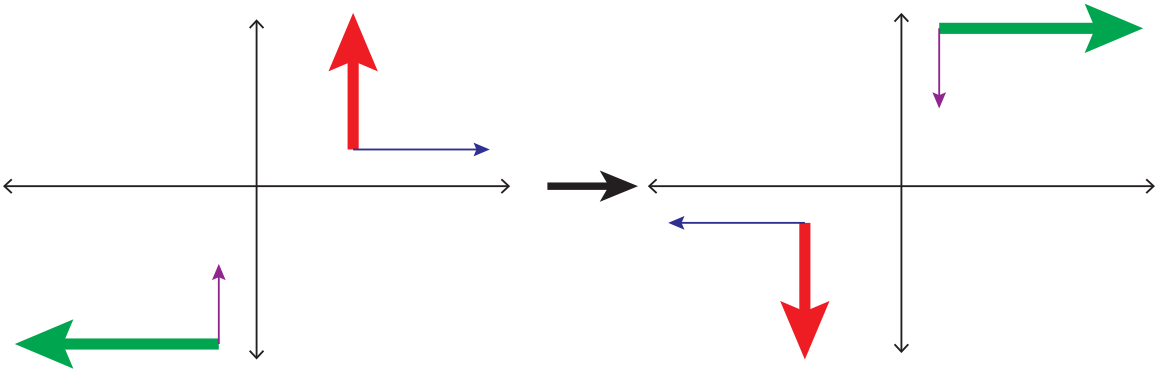

Figure 2.1: A 2D pointwise inversion operation on two sets of vectors according to (2.4).

2.2 Plane Couette Flow

If the domain is limited to $\mathbb{R}^2 \times [-1, 1]$ with the boundary conditions of plane Couette flow, we lose some of the symmetry transformations of the full, unrestricted problem, leaving us with two basic discrete symmetries: a rotation by π about the z axis (denoted σ_x) and a reflection about the z axis (denoted σ_z)[2], together form a discrete symmetry group $D = D_1 \times D_1 = \{e, \sigma_x, \sigma_z, \sigma_{xz}\}$ of order 4, where

$$\sigma_x[u, v, w](x, y, z) = [-u, -v, w](-x, -y, z) \tag{2.5}$$
$$\sigma_z[u, v, w](x, y, z) = [u, v, -w](x, y, -z) \tag{2.6}$$
$$\sigma_{xz}[u, v, w](x, y, z) = [-u, -v, -w](-x, -y, -z) \tag{2.7}$$

The continuous symmetries are the two parameter steamwise-spanwise translations, which, when provided periodic boundary conditions, form a continuous $SO(2) \times SO(2)$ symmetry group

$$\tau(l_x, l_z)[u, v, w](x, y, z) = [u, v, w](x + l_x, y, z + l_z). \tag{2.8}$$

The complete symmetry group is then any combination of these symmetry operations, given by $\Sigma = SO(2)_x \ltimes D_{1,x} \times SO(2)_z \ltimes D_{1,z}$[3].

2.3 Properties and Isotropy Subgroups of Σ

It should be evident that since plane Couette flow is equivariant under the continuous translations given in (2.8), trajectories can be traveling wave equilibria or relative periodic orbits: that is, if one moves into a different reference frame, the trajectory is a regular equilibrium or periodic orbit. However, an initial condition that is fixed by σ_z cannot be translated in the spanwise direction without losing σ_z symmetry (except

[2]The motivation for these subscripts will become apparent shortly
[3]$\ltimes$ is the semidirect product

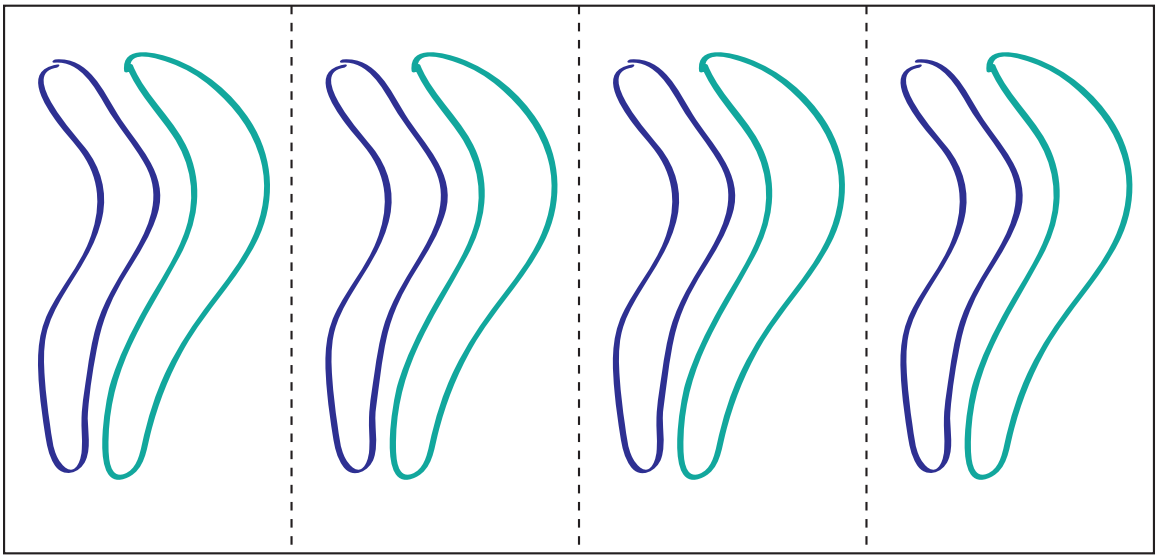

Figure 2.2: If the flow state is fixed by $\tau(\frac{1}{4}L_x, 0)$, then the cell will have four repeating streamwise subcells, and it becomes more efficient to solely consider the subcell.

for the trivial case where $\frac{\partial \mathbf{u}_z}{\partial z} = 0$). Similarly, an initial condition that is fixed by σ_x cannot be translated in the streamwise direction without losing σ_x symmetry (and an initial condition that is fixed by σ_{xz} symmetry cannot be translated at all without losing σ_{xz} symmetry). Since these symmetries are also invariant[4], a trajectory with one of the discrete symmetries cannot be a traveling wave in the direction corresponding to its subscript.

The presence of the periodic boundary conditions also implies that all solutions are fixed by the full-period translation $\tau(L_x, 0)$ and $\tau(0, L_z)$. However, solutions can also be fixed by any rational translation of the form $\tau(aL_x, bL_z)$, where $a, b \in \mathbb{Q}$, or by the continuous translations. If we fix $\mathbf{u}$ by a continuous translation, we force it to have a zero derivative along that axis[5], and such solutions tend to be uninteresting as they are equivalent to low-dimensional problems. If $\mathbf{u}$ is fixed instead by rational translations, the periodic cell is tiled with repeating subcells , as in Figure 2.2. This implies that we can restrict ourselves to full box length translations, which are in any case required by the periodic boundary conditions.

There is one further reason to restrict the translation symmetry - the unrestricted Σ is not an abelian group, as demonstrated in Figure 2.3, so the order of application of symmetry transformations matters in general, which is undesirable, especially when trying to consider the conjugacy classes. From (2.5–2.8) however, it is evident that

[4]That is, if the symmetry is satisfied at time $t = t_0$, it must be satisfied for all times. This is trivially true from Definition 4

[5]That is, if we fix $\mathbf{u}$ by $\tau l_x, 0$ for any real l_x, then $\frac{\partial \mathbf{u}}{\partial x} = 0$, and similarly for z.

the following relation between the σ and τ holds:

$$\sigma_i \tau_i = \tau_i^{-1} \sigma_i, \tag{2.9}$$

where i can index the x,z or xz symmetries. Left-multiplication by τ_i yields

$$\sigma_i \tau_i^2 = \tau_i^{-1} \sigma_i \tau_i. \tag{2.10}$$

If τ_i is restricted to *half*-box shifts, then (2.10) becomes

$$\sigma_i \tau_{i,2}^2 = \sigma_i \tau_{i,1} = \sigma_i = \tau_{i,2}^{-1} \sigma_i \tau_{i,2}, \tag{2.11}$$

where the second subscript on τ represents the spatial periodicity imposed by τ. Right multiplication by $\tau_{i,2}$ yields

$$\tau_{i,2} \sigma_i = \sigma_i \tau_{i,2}. \tag{2.12}$$

So if τ is restricted to half-integer box shifts, $\Sigma_2 \subset \Sigma$ is an abelian group, as demonstrated in Figure 2.4[6]. The subgroups of Σ_2, which form the isotropy subgroups for plane Couette flow, are of order $\{1, 2, 4, 8, 16\}$. There is only one order 1 subgroup: $\{e\}$, which is the typical isotropy group for turbulent flows[7]. There are 15 subgroups of order 2, 35 subgroups of order 4, 15 subgroups of order 8, and one subgroup of order 16, giving 67 subgroups. Luckily, consideration of conjugacy classes greatly lowers the number of subgroups we need to consider. For instance, the subgroups $\{e, \sigma_x\}$ and $\{e, \sigma_x \tau_{x,2}\}$ belong to the same conjugacy class.

Proof. Following Definition 7, choose $a = \tau_{x,4} \in \Sigma$. Then

$$\tau_{x,4}^{-1} \{e, \sigma_x\} \tau_{x,4} = \{\tau_{x,4}^{-1} \tau_{x,4}, \tau_{x,4}^{-1} \sigma_x \tau_{x,4}\} = \{e, \tau_{x,4}^{-1} \sigma_x \tau_{x,4}\}. \tag{2.13}$$

But by (2.10),

$$\{e, \tau_{x,4}^{-1} \sigma_x \tau_{x,4}\} = \{e, \sigma_x \tau_{x,2}\}. \tag{2.14}$$

So $\{e, \sigma_x\}$ and $\{e, \sigma_x \tau_{x,2}\}$ belong to the same conjugacy class. □

So there are only eight conjugacy classes of order 2, with representatives generated by $\tau_x, \tau_z, \tau_{xz}, \sigma_x, \sigma_z, \sigma_{xz}, \sigma_x \tau_z, \sigma_z \tau_x$. The conjugacy classes of pure translations can be disregarded, since they are equivalent to considering smaller cells, so we are left with five order 2 conjugacy classes. Of these, the two generated by σ_x and $\sigma_x \tau_z$ do not permit streamwise traveling waves, the two generated by σ_z and $\sigma_z \tau_x$ do not permit spanwise traveling waves, and one generated by σ_{xz} permits no traveling waves at all. Furthermore, groups of higher order go not have any conjugacy classes that permit symmetry breaking, so we will ignore those groups entirely, although a particular order 4 group, $S = \{e, \sigma_z \tau_x, \sigma_x \tau_{xz}, \sigma_{xz} \tau_z\}$, which has been the isotropy subgroup of many previous results [23], and is used as a starting point for some of the results for this thesis. The important exact coherent structures of this thesis have isotropy subgroups $S_x = \{e, \sigma_x \tau_{xz}\}$ and $S_z = \{e, \sigma_z \tau_{xz}\}$.

[6] Note that this also implies that $\tau_{i,2}$ is its own inverse.

[7] Since it lacks any symmetry.

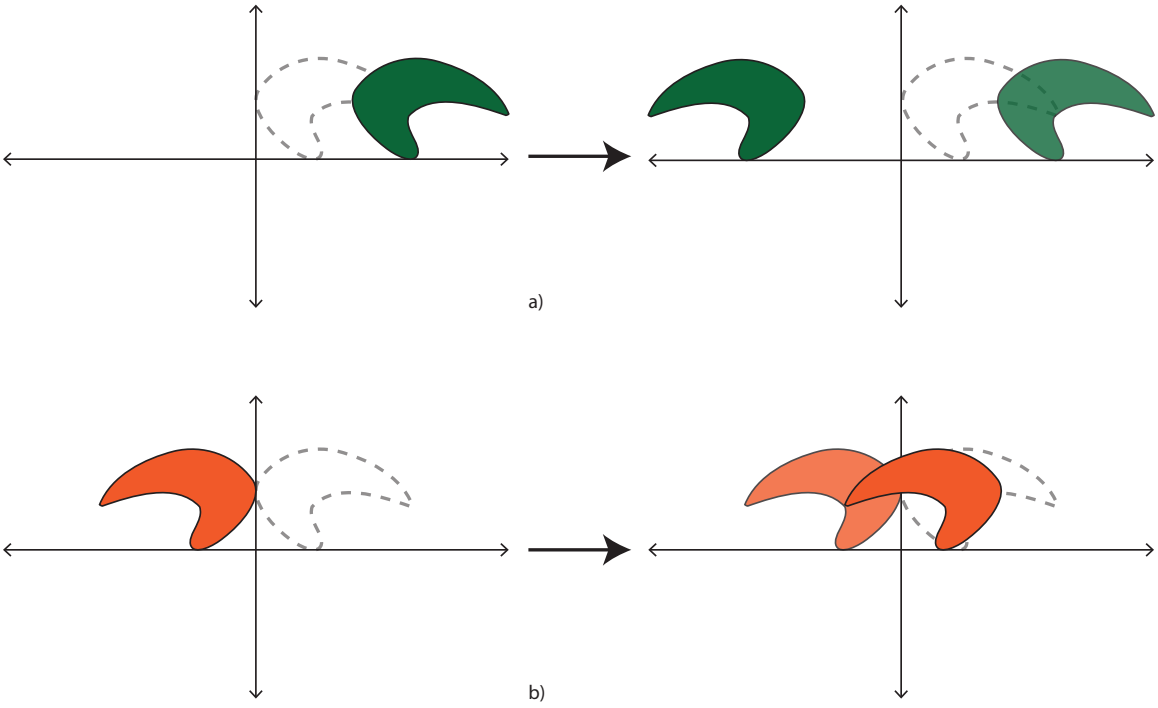

Figure 2.3: A simple demonstration that shifts and reflects do not commute in general. a) shows an object with a dashed outline that is translated to the right, and then reflected across the vertical, while b) shows the same object reflected before it is translated to the right. Notice that the final positions of the object are not the same.

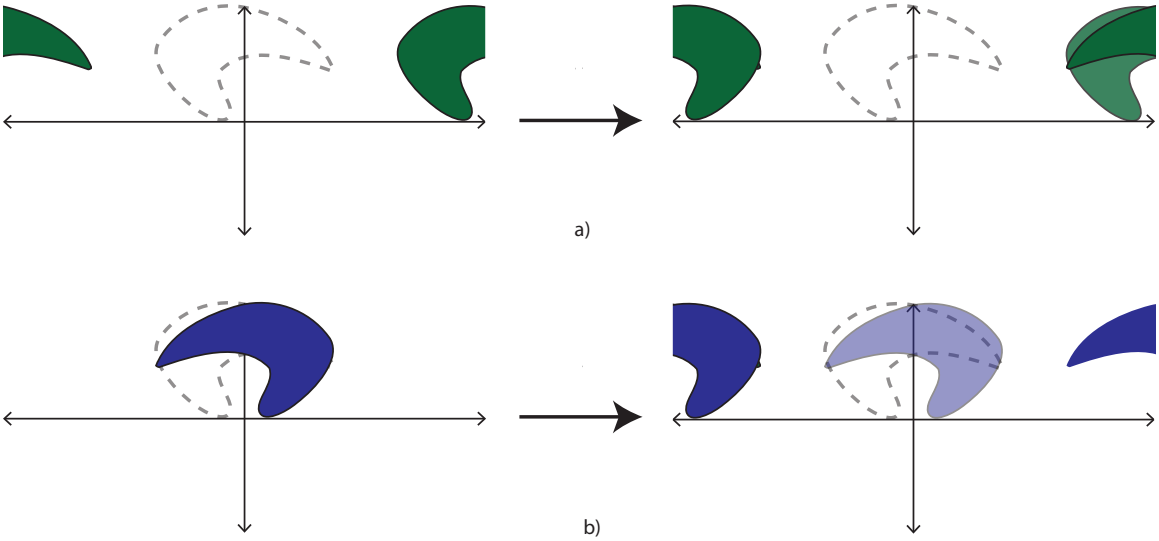

Figure 2.4: When periodic boundary conditions are imposed and translations are fixed to half-period lengths, shifts and reflects commute. a) shows an object that is shifted and then reflected across the vertical, while b) shows the same object reflected across the vertical and then shifted. Notice that the final positions are the same, even if the intermediaries are not.

Chapter 3

Numerics and Workflow

> On two occasions I have been asked, "Pray, Mr. Babbage, if you put into the machine wrong figures, will the right answers come out?" ... I am not able rightly to apprehend the kind of confusion of ideas that could provoke such a question.
>
> Charles Babbage, Passages from the Life of a Philosopher

Computational studies of Navier-Stokes, especially as a dynamical system, are difficult for many reasons, but most important among them is the high degree of complexity inherent in the numerical tools required to maintain efficiency. As mentioned earlier, the two major approaches towards simulating Navier-Stokes are modeling, where some assumptions are made to reduce the difficult of simulation, and direct numerical simulation (DNS), where no assumptions beyond those used to derive Navier-Stokes and set up the boundary conditions are used. DNS is naturally more accurate (since the physicality of some modeling assumptions can be suspect), but since it fully resolves Navier-Stokes, it is significantly more expensive than modeling, and methods that attempt to offset this extra cost tend to be extremely complex. For this reason, I use the open source library `Channelflow` [17], which has been essential in making any headway in this thesis. `Channelflow` is a spectral DNS library, with additional utilities to find, parametrically continue, and analyze exact coherent structures, which I will lay out in some detail below.

3.1 The Spectral Method

3.1.1 The Residual

Spectral methods are, like finite element methods, part of a larger class of numerical methods known as **weighted residual methods**. In this class of methods, functions

are approximated by a truncated series expansion, with the restriction that a quantity related to the residual be zero (instead of the residual itself). The quantity used for the spectral method is the scalar product

$$\langle u, v \rangle_w = \int_a^b uvw \ dx, \tag{3.1}$$

where $u(x), v(x)$ are some functions on the interval $[a, b]$, and $w(x)$ is a weighting function. If we then imagine some platonic function[1] $u(x)$ that we attempt to approximate via a finite series expansion, so that

$$u_N(x) = \sum_{k=0}^{N} \hat{u}_k \psi_k(x), \tag{3.2}$$

for some set of orthogonal basis functions $\psi_k(x)$, then the residual is given by

$$R_N = u(x) - u_N(x), \tag{3.3}$$

and for some differential equation

$$Du = f, \tag{3.4}$$

where D is some arbitrary differential operator and $f(x)$ is some arbitrary source function, the residual is defined

$$R_N = Du_N, \tag{3.5}$$

as expected. While it may seem logical to require $R_N = 0$, this is not possible in general for finite N, so we instead require that for a set of test functions $\phi_i(x)$ and weighting function w^*,

$$\langle R_N, \phi_i(x) \rangle_{w^*} = R_N(x_i) = 0, \tag{3.6}$$

for some set of x_i. If $\phi_i(x) = \delta(x - x_i)$ and $w^* = 1$, then we have the colocation method, which forces the approximation to match the platonic function at a set of points. If $\phi_i(x) = \psi_i(x)$ and $w^* = w$, then we have the Galerkin method, which forces the mean residual to be zero.

3.1.2 Basis Functions

In the spectral method, trigonometric functions are chosen as the basis. The advantage of trigonometric functions over polynomials is the rapid convergence of the series coefficients – the Fourier coefficients converge exponentially fast, so we can achieve extremely high accuracy with a lower number of modes [25].[2] `Channelflow`

[1] That is, the function that is to be approximated.

[2] Spectral methods are inappropriate when the boundary geometry is highly complex, as is the case in the majority of industrial applications, where more general finite element methods are used.

uses Fourier series in the streamwise-spanwise directions, where the basis functions and spectral projection are given by

$$F_k(x) = \mathrm{e}^{ikx} \tag{3.7}$$

$$u_K(x) = \sum_{k=-K}^{K} \hat{u}_k \mathrm{e}^{ikx}, \tag{3.8}$$

and Chebyshev polynomials of the first kind in the wall-normal direction, where the basis functions and spectral projection are given by

$$T_k(x) = \cos\left(k \arccos x\right) \tag{3.9}$$

$$u_N(x) = \sum_{k=0}^{(2k-1)/2} \hat{\mathbf{u}}_k T_k(x). \tag{3.10}$$

The Fourier series expansion is particularly nice since the derivative $\partial_x F_k(x) = ikF(x)$ is especially easy to calculate, as are the Fourier coefficients by virtue of the Fast Fourier Transform, implemented in the Fastest Fourier Transform in the West (FFTW) library [26].

For Chebyshev polynomials, the derivative is slightly more complicated, since

$$\partial_x T_k(x) = 2k \sum_{n=0}^{K} \frac{1}{c_{k-1-2n}} T_{k-1-2n}(x), \tag{3.11}$$

where $c_k = 1$ if $k = 1$ and 2 if $k > 1$. Since the derivative of a single Chebyshev term becomes a sum of Chebyshev terms, the derivative of the Chebyshev representation of a function

$$\partial_x \sum_{k=0}^{N} \hat{\mathbf{u}}_k T_k(x) = \sum_{k=0}^{N} \hat{\mathbf{u}}_k^{(1)} T_k(x), \tag{3.12}$$

$$\hat{\mathbf{u}}_k^{(1)} = \frac{2}{c_k} \sum_{\substack{p=k+1 \\ (p+k)\ \text{odd}}}^{N} p\hat{\mathbf{u}}_p, \quad k \neq N, \tag{3.13}$$

$$\hat{u}_N^{(1)} = 0. \tag{3.14}$$

As with the Fourier decomposition, however, Chebyshev coefficients can be calculated by a discrete cosine transform [18], which is a special case of the discrete Fourier transform, and is thus also computed by FFTW.

While Fourier expansions are the easiest to deal with, they are best used on periodic boundaries, since the imposition of aperiodic boundary conditions on a Fourier series expansion can lead to Gibbs oscillations that can make the simulation aphysical [25]. For this reason, the velocity field is expanded as a Fourier series in the plane,

and as a Chebyshev polynomial in the wall-normal direction. The velocity field is then represented as

$$\mathbf{u}_{KJL}(x,y,z) = \sum_{k=-K}^{K} \hat{u}_k(x)\mathrm{e}^{ikx} \sum_{j=-J}^{J} \hat{u}_j(z)\mathrm{e}^{ijz} \sum_{l=0}^{L} \hat{\mathbf{u}}_l(y)T_l(y). \tag{3.15}$$

3.1.3 Spatio-Temporal Discretization

Under the (Galerkin) spectral approximation

$$\mathbf{u}(x,y,z) = \mathbf{U}_{KJL}(x,y,z), \tag{3.16}$$

the partial differential equation

$$\frac{\partial \mathbf{u}}{\partial t} = f_T(\mathbf{u}), \tag{3.17}$$

becomes an ordinary differential equation (ODE)

$$\frac{\mathrm{d}\mathbf{U_{KJL}}}{\mathrm{d}t} = F_T(\mathbf{U}_{KJL}), \tag{3.18}$$

where $f_T(\mathbf{u})$ is the forward time evolution of the Navier-Stokes equation, and $F_T(\mathbf{U}_{KJL})$ is its spectral approximation via (3.6). The temporal ODE can be solved in any number of ways – `Channelflow` allows the user to choose from several implicit-explicit methods, where the implicit : Crank-Nicolson Forward Euler, Crank-Nicolson Adams-Bashforth, Spalart-Moser Runge-Kutta and Semi-implicit Backwards Differentiation of orders 1 to 4. The order 3 Semi-implicit Backwards Differentiation (SBDF3) was chosen by default, and no reason to change this was anticipated, since SBDF3 is known to have a relatively large time step and low error for large Re [27].

3.2 Newton-Krylov-Hookstep Method

In order to find exact coherent structures it is necessary to solve the equation

$$\mathbf{u} - \sigma f_T(\mathbf{u}) = R_T(\mathbf{u}) = 0, \tag{3.19}$$

which is easiest tackled by root-finding algorithms. The root finding method used by `Channelflow` is based on Newton's method, with some additional refinements.

3.2.1 Newton's Method

The principle behind Newton's method is as follows: Suppose we have $f(x)$ be a smooth and differentiable function, and an initial, 'good' guess x_0 for the root of f.[3]

[3]How good a guess needs to be is highly dependent on the problem. For this thesis, an initial condition that gave $R_T(\mathbf{u}) < 0.001$ was considered a sufficiently good guess.

Then we can find a better guess for the root of f by finding the root of the tangent line at $f(x_0)$ (Figure 3.1). Mathematically,

$$f(x_n) + f'(x_n)\,(x_{n+1} - x_n) = 0, \tag{3.20}$$

$$x_{n+1} = x_n - \frac{f(x_n)}{f'(x_n)}. \tag{3.21}$$

In higher dimensions, (3.20–3.21) are replaced by the matrix equations

$$\mathbf{f}(\mathbf{x}_n) + \mathbb{J}_{f,\mathbf{x_n}}(\mathbf{x}_{n+1} - \mathbf{x}_n) = 0, \tag{3.22}$$

$$\mathbf{x}_{n+1} = \mathbf{x}_n - \mathbb{J}^{-1}_{f,\mathbf{x}_n}\mathbf{f}(\mathbf{x}_n) \tag{3.23}$$

where $\mathbb{J}_{f,\mathbf{x_n}}$ is the Jacobian of the Navier-Stokes equation at $\mathbf{x}_n$.

Newton's method is extremely fast and converges quadratically on the root [28], but is not guaranteed to do so - a simple example is if the n-th guess is at (or very close to) a local minimum, in which case the adjustment term of (3.21) will explode, taking us very far away from the initial, good guess. Furthermore, in a system with around 10^5 unknowns, inverting the Jacobian in (3.22) becomes very time consuming. To speed this up, we can trade off accuracy for speed by replacing (3.22) with a minimization problem

$$||\mathbf{f}(\mathbf{x}_n) + \mathbb{J}_{f,\mathbf{x_n}}\mathbf{dx}_n|| = r_n < \epsilon||\mathbf{f}(\mathbf{x}_n)||, \tag{3.24}$$

where $||\mathbf{x}|| = \sqrt{\mathbf{x}\cdot\mathbf{x}}$ is the norm of $\mathbf{x}$, r_n is the n-th residual, $\mathbf{dx}_n = \mathbf{x}_{n+1} - \mathbf{x}_n$ and ϵ is some small parameter that controls how accurate we want the minimization to be [29]. Note that if $\epsilon = 0$, we recover (3.22). Newton's method can be terminated either when successive steps fail to refine $f(\mathbf{x})$ sufficiently, or when $f(\mathbf{x})$ is sufficiently small.

3.2.2 The Generalized Minimum Residual Method

There are a vast quantity of residual minimization algorithms in existence, each typically optimized for a particular class of problem. `Channelflow` uses the **G**eneralized **M**inimum **RES**idual (GMRES) method, a Krylov subspace method developed in 1986 by Saad and Schultz [30]. To illustrate the principle of GMRES, consider the least squares problem of finding the $\mathbf{x}$ that minimizes

$$||\mathbb{A}\mathbf{x} - \mathbf{b}|| = r. \tag{3.25}$$

3.2.2.1 The Krylov Subspace

Instead of searching for $\mathbf{x}$ in the full vector space of the problem, Krylov methods restrict the space to a **Krylov subspace**. The k-th Krylov subspace for a matrix $\mathbb{A}$ and a vector $\mathbf{c}$, with a guess $\mathbf{x}_0$ is defined

$$\mathcal{K}_k(\mathbb{A}, \mathbf{c}) = \text{span}\left(\mathbf{c}, \mathbb{A}\mathbf{c}, \mathbb{A}^2\mathbf{c}..., \mathbb{A}^{k-1}\mathbf{c}\right). \tag{3.26}$$

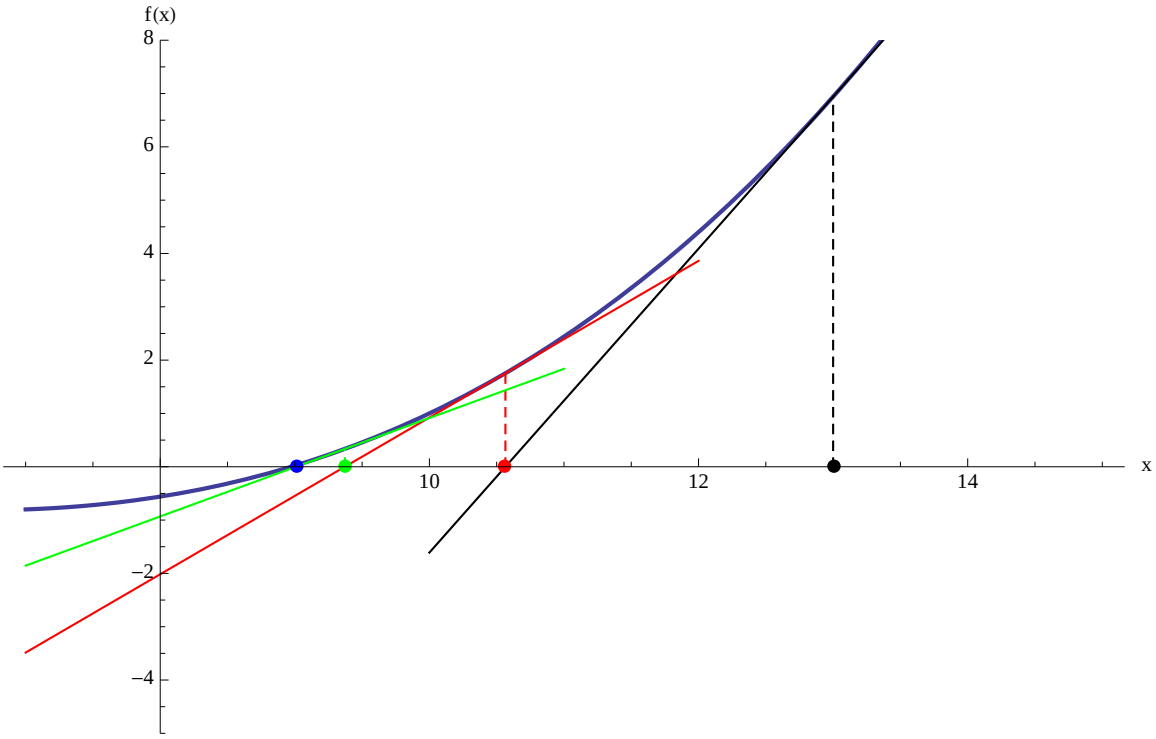

Figure 3.1: A demonstration of Newton's method in 1D on a simple function with the root at $x_r \approx 8.98$. Starting at $x_0 = 13$, the method converges to within 10^{-4} in just three steps.

In practice, $\mathbf{c}$ is often set to equal $\mathbf{b} - \mathbb{A}\mathbf{x}_0$, since it allows for the calculation of convergence estimates. [31]. The motivation for searching for the solution to (3.25) in the Krylov subspace can be made clear if we consider a slight rearrangement of (3.25),

$$\mathbf{x} = \mathbb{A}^{-1}\mathbf{b}, \tag{3.27}$$

from which it is clear that if $\mathbb{A}^{-1}$ can be written as a power series of $\mathbb{A}$, $\mathbf{x}$ lies in the Krylov subspace. This can be shown via consideration of the characteristic polynomial of $\mathbb{A}$, and is proved in [31].

3.2.2.2 The Arnoldi Iteration

Unfortunately, the set of vectors generated by (3.26) is not guaranteed to form an orthonormal basis, so in practice the Krylov subspace is generated via Algorithm 1, known as the **Arnoldi Iteration**.

Algorithm 1. Begin with $\mathbf{q}_1 = \mathbf{b} - \mathbb{A}\mathbf{x}_0$. Then for the k-th Arnoldi iteration,

1. calculate $h_{ij} = \mathbb{A}\mathbf{q}_i \cdot \mathbf{q}_j$, for $i = 1, 2, ..., j$,

2. generate $\mathbf{p} = \mathbb{A}\mathbf{q}_j - \sum_{i=1}^{j} h_{ij}\mathbf{q}_i$,

3. and normalize $\mathbf{q}_{j+1} = \dfrac{\mathbf{p}}{||p||}$,

for $j = 1, 2, ..., k$.

Incidentally, the Arnoldi iteration is in general used to solve the eigenvalue problem for a matrix[4], which will prove to be useful later. If we let $\mathbb{Q}_k = [\mathbf{q}_1|\mathbf{q}_2|...|\mathbf{q}_k]$, and $[\mathbb{H}_k]_{ij} = h_{ij}$ if h_{ij} exist, and 0 otherwise, then

$$\mathbb{H}_k = \mathbb{Q}_k^* \mathbb{A} \mathbb{Q}, \tag{3.28}$$

and

$$\mathbb{A}\mathbb{Q}_k = \mathbb{Q}_{k+1} \tilde{\mathbb{H}}_k, \tag{3.29}$$

where $\tilde{\mathbb{H}}_k$ is $\mathbb{H}_k$ with an additional row $[0, 0, 0..., h_{k+1,k}]$. Following the derivation in [31], if $\mathbf{z} \in \mathcal{K}_k(\mathbb{A}, \mathbf{c})$,

$$\mathbf{z} = \mathbb{Q}_k \mathbf{y}, \tag{3.30}$$

for some $\mathbf{y}$. Then

$$\begin{aligned} \mathbb{A}\mathbf{z} &= \mathbb{A}\mathbb{Q}_k \mathbf{y}, \\ &= \mathbb{Q}_{k+1} \tilde{\mathbb{H}}_k \mathbf{y}, \end{aligned} \tag{3.31}$$

and

$$\begin{aligned} \mathbf{c} &= ||\mathbf{b} - \mathbb{A}\mathbf{x}||\mathbf{q}_1, \\ &= ||\mathbf{b} - \mathbb{A}\mathbf{x}||\mathbf{q}_1, \\ &= ||\mathbf{b} - \mathbb{A}\mathbf{x}||\mathbb{Q}_{k+1}\mathbf{e}_1, \end{aligned} \tag{3.32}$$

where $\mathbf{e}_1$ is the first standard basis vector. This changes the least squares problem from finding the $\mathbf{x}$ that minimizes (3.25) to the $\mathbf{y}$ that minimizes

$$|| \left(||\mathbf{b} - \mathbb{A}\mathbf{x}|| \right) \mathbf{e}_1 - \tilde{\mathbb{H}}_k \mathbf{y}|| = r, \tag{3.33}$$

and is solved by Algorithm 2.

Algorithm 2. Begin with

$$\begin{aligned} \mathbf{c} &= \mathbf{b} - \mathbb{A}\mathbf{x}_0, \\ \mathbf{q}_1 &= \frac{\mathbf{c}}{||c||}, \\ \mathbb{Q}_1 &= \mathbf{q}_1, \\ \mathcal{K}_1(\mathbb{A}, \mathbf{c}) &= \text{span}(\mathbf{q}_1). \end{aligned}$$

Then the k-th GMRES iteration is given by

1. generating $\mathbf{q}_{k+1}$, $\mathbb{Q}_{k+1}$ and $\tilde{\mathbb{H}}_k$ via the Arnoldi iteration,

[4]That is, solving for the eigenvectors $\mathbf{q}_k$ and eigenvalues λ_k that satisfy $\mathbb{A}\mathbf{q}_k = \lambda_k \mathbf{q}_k$

2. finding the $\mathbf{y}_{k+1}$ that minimizes (3.33),

3. and computing $\mathbf{x}_{k+1} = \mathbb{Q}_{k+1}\mathbf{y}_{k+1}$.

The second step of Algorithm 2 may seem nonsensical - why have we put this much effort into getting an equation similar to (3.25)? The key lies in realizing that the minimization problem in Algorithm 2 has a dimension of k, whereas (3.25) has a dimension on the order of 10^5. Since the matrix inversion problem scales as dimension to the third power, this reduction is extremely powerful – especially since GMRES converges quickly – in this thesis, GMRES rarely took more than 20 iterations to converge. The minimization step in Algorithm 2 can be solved via a QR decomposition, with a time complexity of $O(n)$ [32].

3.2.3 The Hookstep

While Newton's method is incredibly powerful, it needs to be provided a sufficiently good guess to stand a chance of converging to a solution. However, in practice, we may be limited in our ability to provide good guesses with our computing resources, and thus need a method of dealing with less than ideal guesses. One major issue with a suboptimal guess is that the linear model used in deriving Newton's method may not be valid for the Newton step $\mathbf{dx}_N$, as in Figure 3.2.

If this is the case, switching to a constrained **hookstep** can force the algorithm to take artificially smaller steps, until the linear model becomes locally accurate. In `Channelflow`, the equation of constraint for the hookstep $\mathbf{dx}_H$ is

$$||\mathbf{dx}_H|| \leq \delta, \tag{3.34}$$

where δ is the **trust region** of the linear model, which is recomputed whenever the linear model changes significantly. The hookstep is further restricted to lie in the k-th Krylov subspace, so that

$$\mathbf{dx}_H = \mathbb{Q}_k\mathbf{s}, \tag{3.35}$$

where $\mathbf{s}$ is now the k-dimensional step we need to take. As with the Newton step, the hookstep is determined using GMRES. Unlike the Newton step, the minimization stage of Algorithm 2 is not computed via the QR decomposition [17]. Instead, we substitute (3.29) and (3.35) into (3.25), giving the residual which we wish to minimize with respect to $\mathbf{s}$,

$$||\mathbb{Q}_{k+1}^T\mathbf{b} - \tilde{\mathbb{H}}_k\mathbf{s}|| = r. \tag{3.36}$$

Applying the singular value decomposition $\tilde{\mathbb{H}}_k = \mathbb{U}\mathbb{D}\mathbb{V}^T$ transforms (3.36) intro

$$||\hat{\mathbf{b}} - \mathbb{D}\hat{\mathbf{s}}|| = r, \tag{3.37}$$

where $\hat{\mathbf{s}} = \mathbb{V}^T\mathbf{s}$, $\hat{\mathbf{b}} = \mathbb{U}^T\mathbb{Q}_{k+1}^T\mathbf{b}$, $\mathbb{U}, \mathbb{V}$ are square, unitary matricides and $\mathbb{D}$ is a rectangular diagonal matrix. Using Lagrange multipliers, the minimization problems yields the solution [17]

$$\hat{s}_i = \frac{\hat{b}_i D_{ii}}{D_{ii}^2 + \mu}, \tag{3.38}$$

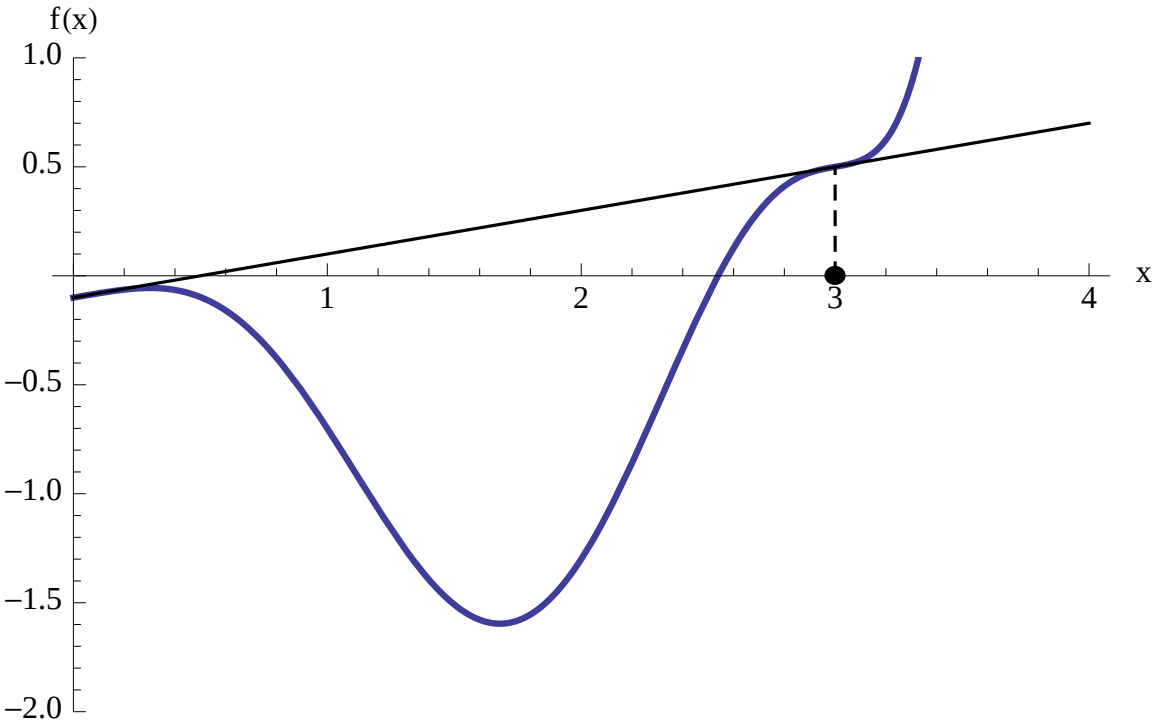

Figure 3.2: If we assume the linear model remains valid for the entire step, we can sometimes be led astray. Because the function becomes rapidly nonlinear, the Newton step takes us very far away from the actual root we are trying to find, and will likely never converge.

where μ minimizes

$$||\hat{\mathbf{s}}(\mu)||^2 - \delta^2 = \mathfrak{r}, \tag{3.39}$$

which can be trivially solved by a 1D Newton method.

3.3 Recurrence Diagrams

While the augmentation of the Newton-Krylov method by the hookstep makes it more resilitent against poor guesses, the Newton-Krylov-Hookstep (NKH) method remains extremely sensitive to initial conditions. As a result, an method to generate decent guesses to kickstart the NKH solver is vital. The method used in this thesis is as follows:

The key here is then to find an intelligent low dimensional projection. One possibility is to view the trajectory in the dissipation and energy input plane, as in [14], which has proven successful in the past. A better approach, however, is to consider the **recurrence diagram** of the trajectory, which can be generated via Algorithm 3.

Algorithm 3.

1. Begin with an initial condition. This can be chosen by randomly generating a field, or making a slight random perturbation off a known exact coherent structures.

2. Integrate this initial condition forward in time using SBDF3 to obtain a trajectory

3. Project this trajectory into some low dimensional basis which naturally provides insight into the dynamical structure

4. Extract some number of good guesses from this projection, and pass them along to the NKH solver.

The recurrence diagram of a trajectory is a method by which the spatio-temporal separation of successive flow states in a trajectory can be visually and numerically analyzed. The recurrence diagram is a 2D plot of the values of the function

$$\mathfrak{R}(t,T) = ||\mathbf{u}(t+T) - \mathbf{u}(t)||, \tag{3.40}$$

where minima of $\mathfrak{R}$ may indicate the existence of exact coherent structures. Interpretation of a recurrence diagram is not an exact science - for example, a naive search for the minimum of Figure **??**[5] would yield all the points for which $T = 0$. Experience has shown that long, horizontal streaks of minima correspond to the shadowing of a periodic orbit, and tend to be excellent sources of good guesses for the NKH solver.

When streamwise or spanwise symmetry is broken, (3.40) must be modified to allow for the possibility of relative solutions, as the problem now changes to finding minima of

$$\mathfrak{R}(t,T,l_x,l_z) = ||\tau(l_x,l_z)\mathbf{u}(t+T) - \mathbf{u}(t)||. \tag{3.41}$$

In principle this is now a 3 or 4 dimensional minimization problem, which would normally preclude the use of a visual approach. This issue is resolved by searching for the (l_x, l_z) that minimizes (3.41) for each (t, T), and only plotting those values of $\mathfrak{R}$. Note that time cost of generating the recurrence diagram goes from $O(n^2)$ to $O(n^4)$ as the spanwise and streamwise symmetries are broken. As a result, analyzing the trajectory of a completely asymmetric trajectory is extremely computationally costly.

3.4 Parametric Continuation

If we have a solution to (3.19) for some control parameters, such as Re or the cell size, we may wish to see how these solutions vary with these control parameters. For example, if we know that a solution S exists for $Re = 400$, we might want to know how this solution differs from the solution , S' at $Re = 200$, assuming that S' exists.

[5] I currently don't have MATLAB, Mathematica or Illustrator, so I'll get these figures done as soon as my laptop gets back. Should be by Monday

The solution may, for example vary as in Figure 3.3 One of the most efficient ways to find these solutions is via Algorithm 4, known as **parametric continuation**.

Algorithm 4. If we have a solution S_{μ_0} with a control parameter μ_0, some solution finding method $\mathfrak{S}(S, \mu)$, then S_{μ_k} can be found by

1. choosing a $\mu_{i+1} = \mu_i + \mathrm{d}\mu$ such that the residual $\mathfrak{S}(S_{\mu_i}, \mu_{i+1})$ is small,
2. and then using S_{μ_i} as a guess for $\mathfrak{S}$ to find $S_{\mu_{i+1}}$,

for $i = 1, 2, .., k - 1$.

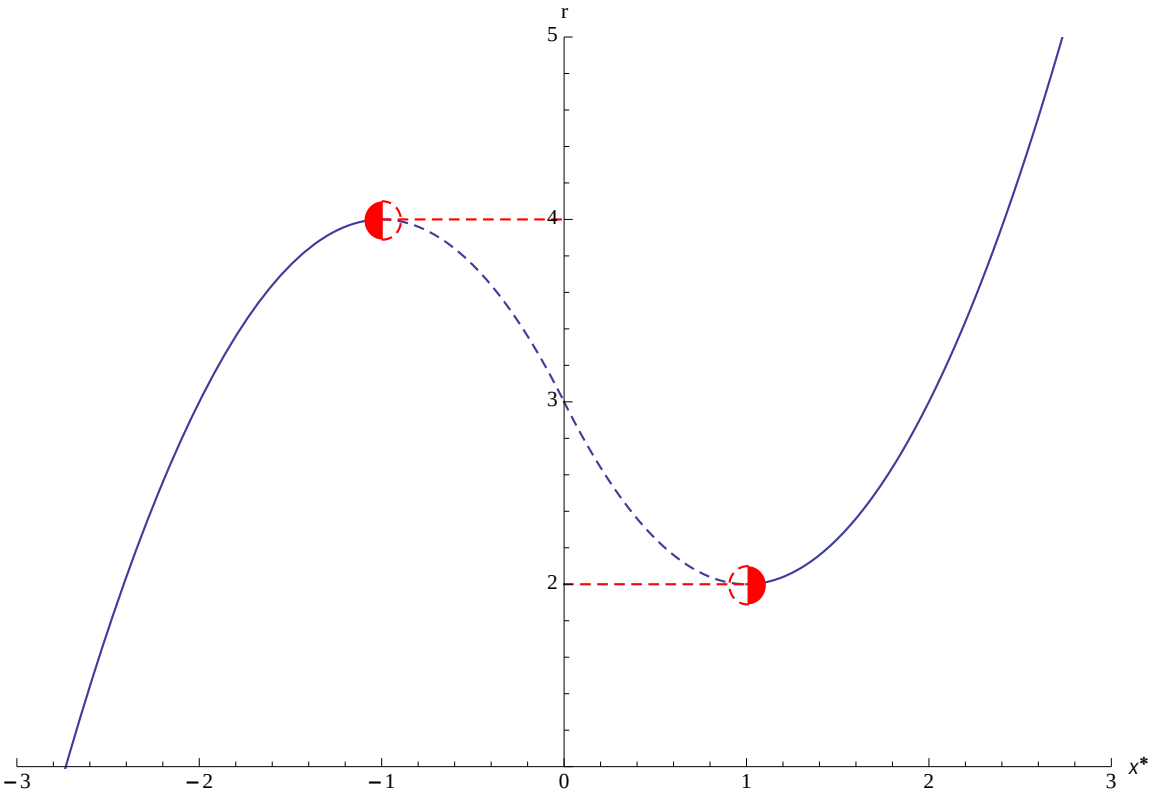

Figure 3.3: A schematic of a 1D bifurcation, that shows the variation of a solution x^* as a function of a control parameter r. While the control parameter $r < 2$, there is only one, stable solution, on the left. At a critical value $r = 2$, however, a new solution emerges at $x^* = 1$ in a **saddle-node bifurcation**. When $2 < r < 4$, the saddle-node splits into two, producing a stable solution (solid) on the right, and an unstable solution (dashed) on the left. As r approaches 4, the original stable solution and the new unstable solution approach each other until at $r =$, they annihilate in another saddle node bifurcation, leaving only the new stable solution.

References

[1] K.-S. Choi, "Fluid dynamics: The rough with the smooth," *Nature*, vol. 440, no. 7085, pp. 754–754, 2006.

[2] P. Grassberger and I. Procaccia, "Measuring the strangeness of strange attractors," in *The Theory of Chaotic Attractors*, pp. 170–189, Springer, 2004.

[3] M. Nagata, "Three-dimensional finite-amplitude solutions in plane couette flow: bifurcation from infinity," *J. Fluid Mech.*, vol. 217, pp. 519–527, 1990.

[4] D. Borrero, "Subcritical transition to turbulence in taylor-couette flow," 2014.

[5] F. Daviaud, J. Hegseth, and P. Bergé, "Subcritical transition to turbulence in plane couette flow," *Phys. Rev. Lett.*, vol. 69, pp. 2511–2514, Oct. 1992.

[6] S. Pope, *Turbulent Flows*. Cambridge University Press, 2000.

[7] E. Hopf, "A mathematical example displaying features of turbulence," *Commun. Pure Appl. Math.*, vol. 1, no. 4, pp. 303–322, 1948.

[8] C. Foias, G. R. Sell, and R. Temam, "Inertial manifolds for nonlinear evolutionary equations," *Journal of Differential Equations*, vol. 73, no. 2, pp. 309–353, 1988.

[9] E. N. Lorenz, "Deterministic nonperiodic flow," *Journal of the atmospheric sciences*, vol. 20, no. 2, pp. 130–141, 1963.

[10] N. Aubry, P. Holmes, J. L. Lumley, and E. Stone, "The dynamics of coherent structures in the wall region of a turbulent boundary layer," *Journal of Fluid Mechanics*, vol. 192, pp. 115–173, 7 1988.

[11] O. Dauchot and N. Vioujard, "Phase space analysis of a dynamical model for the subcritical transition to turbulence in plane couette flow," *The European Physical Journal B-Condensed Matter and Complex Systems*, vol. 14, no. 2, pp. 377–381, 2000.

[12] F. Waleffe, "Exact coherent structures in channel flow," *Journal of Fluid Mechanics*, vol. 435, pp. 93–102, 5 2001.

[13] G. Kawahara and S. Kida, "Periodic motion embedded in plane couette turbulence: regeneration cycle and burst," *J. Fluid Mech.*, vol. 449, pp. 291–300, 2001.

[14] D. Viswanath, "Recurrent motions within plane couette turbulence," *J. Fluid Mech.*, vol. 580, pp. 339–358, 2007.

[15] B. Hof, A. de Lozar, D. J. Kuik, and J. Westerweel, "Repeller or attractor? selecting the dynamical model for the onset of turbulence in pipe flow," *Phys. Rev. Lett.*, vol. 101, p. 214501, Nov 2008.

[16] J. F. Gibson, J. Halcrow, and P. Cvitanović, "Visualizing the geometry of state space in plane couette flow," *Journal of Fluid Mechanics*, vol. 611, pp. 107–130, 2008.

[17] J. F. Gibson, "Channelflow: A spectral Navier-Stokes simulator in C++," tech. rep., U. New Hampshire, 2014. `Channelflow.org`.

[18] J. J. Halcrow, *Charting the state space of plane Couette flow: Equilibria, relative equilibria, and heteroclinic connections*. ProQuest, 2008.

[19] R. Granger, *Fluid Mechanics*. Dover Books on Physics Series, Dover Publications, 1995.

[20] S. L. Fischer and S. P. Fischer, "Mean corpuscular volume," *Archives of Internal Medicine*, vol. 143, no. 2, pp. 282–283, 1983.

[21] C. Clarke and B. Carswell, *Principles of astrophysical fluid dynamics*. Cambridge University Press, 2007.

[22] J. Rotman, *An Introduction to the Theory of Groups*. Graduate Texts in Mathematics, Springer, 1995.

[23] J. F. Gibson, J. Halcrow, and P. Cvitanovic, "Equilibrium and travelling-wave solutions of plane couette flow," *Journal of Fluid Mechanics*, vol. 638, pp. 243–266, Nov. 2009.

[24] U. Frisch, *Turbulence: the legacy of A.N. Kolmogorov*. Cambridge University Press, 1995.

[25] R. Peyret, *Spectral methods for incompressible viscous flow*, vol. 148. Springer Science & Business Media, 2002.

[26] M. Frigo and S. G. Johnson, "FFTW: An adaptive software architecture for the FFT," in *Acoustics, Speech and Signal Processing, 1998. Proceedings of the 1998 IEEE International Conference on*, vol. 3, pp. 1381–1384, IEEE, 1998.

[27] U. M. Ascher, S. J. Ruuth, and B. T. Wetton, "Implicit-explicit methods for time-dependent partial differential equations," *SIAM Journal on Numerical Analysis*, vol. 32, no. 3, pp. 797–823, 1995.

[28] W. H. Press, *Numerical recipes 3rd edition: The art of scientific computing*. Cambridge university press, 2007.

[29] R. S. Dembo, S. C. Eisenstat, and T. Steihaug, "Inexact newton methods," *SIAM Journal on Numerical analysis*, vol. 19, no. 2, pp. 400–408, 1982.

[30] Y. Saad and M. H. Schultz, "Gmres: A generalized minimal residual algorithm for solving nonsymmetric linear systems," *SIAM Journal on scientific and statistical computing*, vol. 7, no. 3, pp. 856–869, 1986.

[31] I. C. Ipsen and C. D. Meyer, "The idea behind krylov methods," *American Mathematical Monthly*, pp. 889–899, 1998.

[32] L. N. Trefethen and D. Bau III, *Numerical linear algebra*, vol. 50. Siam, 1997.

[33] S. Taneda, "Experimental investigation of the wake behind a sphere at low reynolds numbers," *Journal of the Physical Society of Japan*, vol. 11, no. 10, pp. 1104–1108, 1956.